DEPARTAMENT DE FÍSICA

Search for weak dipole moments of the τ lepton with the ALEPH detector [1]

María del Pilar Casado Lechuga
Departament de Física, Edifici Cn
Universitat Autònoma de Barcelona
Institut de Física d'Altes Energies
E-08193 Bellaterra (Barcelona)

March 2001

[1] Ph.D. Dissertation

Acknowledgements

I would like to thank Enrique Fernández, my thesis advisor, very much, for all the help, support and knowledge I have received from him. It has been for me a real pleasure to work with him, learning from his experience, his critic way of thinking and his enthusiastic approach of solving problems. My gratitude also for the confidence he has always deposited on me.

My acknowledgement also to Matteo Cavalli–Sforza, for the possibility he offered me of joining the TILECAL collaboration. He also guided me in my master–thesis, having the great luck of learning from his methodical and precise way of doing things. I enjoyed working with him, remembering those days very gratifying.

My very sincere gratitude to Mokhtar Chmeissani for his continuous support, encouragement and help, and for the nice hours spent working together either for BCAL or for the student experiments in the lab. I have learnt from him many things. Among them, the importance of being well determined in your decisions.

I am indebted to Federico Sánchez for the suggestion of this thesis topic. Also for his help and motivation in the initial steps of the work. I also learnt many things working very closely to him for the BCAL DAQ. After he left, my acknowledgement to him for his fast answers by e–mail and for his encouraging comments.

In the final part of the analysis, I have had many fruitful discussions with Frederic Teubert. Many thanks to him for his help during the last steps of the method and the last measurements. I also have to thank him for his kindness and patience answering all my questions about TILECAL in my first years in the institute.

I also received very appreciate help from Ricard Alemany, to introduce in this analysis all the algorithms previously used in ALEPH. He patiently shared with me his experience on tau physics at LEP I.

I want to mention Inkyu Park for his help in the initial steps of the work, while he was at the IFAE, explaining to me whatever technical problems I found in tau physics.

The help of LLuïsa Mir has been also very important. She has tried to understand the problems I encountered and has always helped me very efficiently. I have also to thank her for the organization of the ALEPH meetings at the institute.

I would like to thank some other ALEPH people. First, Henri Videau, the convener of the tau group, for his enthusiastic support on the analysis. And also Gerardo Ganis, Brigitte Bloch–Devaux, Irène Nicolic, Christoph Geweniger, Michel Davier and Laurent Duflot for answering in-conditionally all my questions.

I have had a great luck being able to discuss with world experts in theoretical tau

physics. I want to express my gratitude to José Bernabéu for his support and very useful comments. Also, thanks to Toni Pich, Jordi Vidal and Arcadi Santamaria.

I am indebted to all the ALEPH components of the institute, because I have learnt from all of them in the ALEPH meetings. I want to mention Manel Martí nez, Eugeni Graugés, Gonzalo Merino, Sí lvia Bravo, Hugo Ruí z and Javier López.

Many thanks also to Andreu Pacheco, Martine Bosman, Ramon Miquel and Lluí s Garrido, some of the the seniors of the IFAE. They always provided me their advise and help when I needed.

My gratitude to Pere Mató for his help and advise when it was needed for BCAL. Thanks also to the ALEPH ONLINE people for their efficient answers.

I want to thank my office–mate Hugo also for his friendship and support. And for the comfortable and working atmosphere of the office.

My gratitude also to many people who are now in the IFAE or have been at before. I have received many, many things from all of them: friendship, support, knowledge,... I would like to mention Imma Riu, Sí lvia Bravo, Anna Pascual, Aurelio Juste, Cristóbal Padilla, Gaelle Boix, Eduardo Bartolomé, Xavier Llopart, Oscar Blanch, Mireia Dosil, Laia Cardiel, David Paneque, Pepe Flix,...

Thanks also to the youngest components of the IFAE, many of which have been my own students. My special gratitude to Olga Norniella, Eva Domingo and Xavier Espinal, for their enthusiasm, kindness and interest.

My friends and family have played a very important role in this business. I want to thank my friend Celia for her support and understanding. And also my friend and high school teacher Esperanza Pereda for her dedication and confidence on me.

My warmer gratitude to my brother Manolo for his encouragement, to my sister Anna for her support, to Carme and Marí a Pilar for their love and profitable talks. My indebtedness to my late father and grand–father, and to my mother and grand–mother can not be express with words. What I am is mostly due to them.

Finally, special acknowledgement to my friend and husband Ernest. He is probably the person who has heard more about this thesis. Many thanks for his patience, love, support and friendship.

To Ernest.

Resum

Els moments dipolars febles del leptó tau han de ser zero dins del Model Estàndard, excepte per correccions quàntiques. Aquí explorem possibles desviacions de les components reals i imaginàries del moment dipolar feble magnètic i del moment dipolar feble elèctric (el qual és un terme que viola CP), és a dir $\Re(\mu_\tau)$, $\Im(\mu_\tau)$, $\Re(d_\tau)$ i $\Im(d_\tau)$. ALEPH ja va publicar resultats sobre $\Re(d_\tau)$. Tanmateix, els altres termes es mesuren ara per primer cop. Fem servir 155 pb^{-1} de dades agafades pel detector ALEPH des de 1990 fins a 1995. Els quatre termes s'extreuen simultàniament mitjançant la minimització de la funció de versemblança, construïda a partir de la secció eficaç diferencial total. Els vectors de polarització del tau es recuperen amb polarímetres que són diferents per cada canal. No s'han trobat indicis de física nova i posem els següents límits amb un 95% de nivell de confiança: $|\Re(\mu_\tau)| < 1.34 \times 10^{-3}$, $|\Im(\mu_\tau)| < 2.02 \times 10^{-3}$, $|\Re(d_\tau)| < 4.62 \times 10^{-18}$e cm i $|\Im(d_\tau)| < 8.29 \times 10^{-18}$e cm.

Summary

The weak dipole moments of the tau lepton are expected to be zero within the SM prediction, except for quantum corrections. We explore here possible deviations for the real and imaginary components of both the weak magnetic and the CP–violating weak electric dipole moments, i.e. $\Re(\mu_\tau)$, $\Im(\mu_\tau)$, $\Re(d_\tau)$ and $\Im(d_\tau)$. ALEPH already published results on $\Re(d_\tau)$. However, the other terms are determined here for the first time. We use 155 pb^{-1} of data taken by the ALEPH detector from 1990 to 1995. The four terms are extracted simultaneously by a likelihood fit built from the full differential cross section. The tau polarisation vectors are recovered with polarimeters differing for each decay topology. No signs of new physics have been found and we set the following bounds at 95% CL: $|\Re(\mu_\tau)| < 1.34 \times 10^{-3}$, $|\Im(\mu_\tau)| < 2.02 \times 10^{-3}$, $|\Re(d_\tau)| < 4.62 \times 10^{-18}\,\mathrm{e\,cm}$, and $|\Im(d_\tau)| < 8.29 \times 10^{-18}\,\mathrm{e\,cm}$.

Contents

1 Introduction **1**

2 Theoretical framework **3**
2.1 Formalism for $Z \to \tau^+\tau^-$ production 3
2.1.1 Lorentz structure of $Z \to \tau^+\tau^-$ 3
2.1.2 Theoretical expectations within the SM 6
2.1.3 The Cross Section 6
2.1.4 The cross section terms 8
2.2 Tau decay 13
2.3 Final combined cross section and likelihood fitting 15

3 Description of the experiment **18**
3.1 The LEP collider 18
3.2 The ALEPH detector 21
3.2.1 VDET 23
3.2.2 ITC 24
3.2.3 TPC 26
3.2.4 ECAL 29
3.2.5 HCAL and Muon Chambers 30
3.3 The trigger system 32
3.4 Data Acquisition System and Event Reconstruction 34

4 Algorithms for τ physics **37**
4.1 The tau event selection 37
4.1.1 Selection criteria for rejection of non–tau events 38
4.1.2 Selection efficiency 39
4.2 Charged particle identification (TAUPID) 40
4.3 π^0 Identification (PEGASUS) 41
4.3.1 Photon identification 41
4.3.2 π^0 reconstruction 43
4.4 Tau decay classification (TOPCLAS) 46
4.5 Selection efficiencies and candidates 47
4.6 Monte Carlo and detector simulation 47

4.7 Tau direction of flight 49

5 Likelihood function **52**
5.1 Likelihood formalism 52
5.2 Smearing functions 54
5.3 Detection Efficiency 59
5.4 Effective $\tilde{H}$ functions 63
5.5 Background 66
5.6 Likelihood function summary 71

6 Systematic errors and results **75**
6.1 Calibration curves 75
6.2 Likelihood results 76
6.3 Systematic checks 82
6.4 Systematic uncertainties 83
6.5 Final results and comparison with other experiments 89

7 Summary and Conclusions **95**

A Cross section explicit expression **98**

B Elements for the decay process **102**
B.0.1 Decay into one pion 102
B.0.2 Decay into two pions 103
B.0.3 Decay into three pions 105

List of Figures

2.1 Coordinate system to describe the τ production 7

3.1 The LEP ring and the 4 interaction points 20
3.2 The LEP acceleration chain 21
3.3 The ALEPH detector 24
3.4 The VDET configuration 25
3.5 An overall view of the ITC 25
3.6 Overall view of the TPC 26
3.7 The TPC end–plates and sectors 27
3.8 Detail of a TPC sector edge 28
3.9 Overall view of ECAL 29
3.10 A stack layer of ECAL 30
3.11 Overall view of HCAL 31
3.12 Scheme of the DAQ 36

4.1 Fractions of resolved and unresolved π^0's and single photon as a function of the π^0 energy 44
4.2 Energy resolution of the exclusive π^0's as a function of energy 45
4.3 Invariant mass for two of the classes of this analysis 46
4.4 Geometric view of the τ flight direction reconstruction 50

5.1 Smearing function of the W variable for the ρ channel 56
5.2 Smearing functions of $\cos\theta_h$ for the π channel 57
5.3 Smearing functions of $\cos\theta_h$ for the ρ channel 58
5.4 Smearing functions of $\cos\theta_h$ for the $\pi 2\pi^0$ channel 59
5.5 Smearing functions of $\cos\theta_h$ for the 3π channel 60
5.6 Smearing functions of ϕ_h for the π channel 61
5.7 Smearing functions of ϕ_h for the ρ channel 62
5.8 Smearing functions of ϕ_h for the $\pi 2\pi^0$ channel 63
5.9 Smearing functions of ϕ_h for the 3π channel 64
5.10 Efficiency matrix in the barrel 65
5.11 Efficiency matrix in the end–cap 66
5.12 Efficiencies for contamination of tau background 67
5.13 Smearing functions of the W for the ρ $\pi 2\pi^0$ mixing 69

5.14 Smearing functions of $\cos\theta_h$ for the mis–identification of ρ into $\pi 2\pi^0$ 70
5.15 Smearing functions of $\cos\theta_h$ for the mis–identification of $\pi 2\pi^0$ into ρ 71
5.16 Smearing functions of ϕ_h for the mis–identification of ρ into $\pi 2\pi^0$ 72
5.17 Smearing functions of ϕ_h for the mis–identification of $\pi 2\pi^0$ into ρ 73
5.18 $D_{other\,\rho}(\cos\theta_h - \cos\theta_h^{(0)})$, $D_{other\,\rho}(\phi_h - \phi_h^{(0)})$ and $D_{other\,\rho}(W - W^{(0)})$ 74

6.1 Calibration plots for the π–π channel 78
6.2 First results on the weak magnetic dipole moment channel by channel 79
6.3 First results on the weak electric dipole moment channel by channel 80
6.4 Comparison of the $\cos\theta_h$ distribution for the data and the Monte Carlo simulation 83
6.5 Comparison of the ϕ_h distribution for the data and the Monte Carlo simulation in the π channel 84
6.6 Comparison of the ϕ_h distribution for the data and the Monte Carlo simulation in the ρ channel 85
6.7 Comparison of the ϕ_h distribution for the data and the Monte Carlo simulation in the $\pi 2\pi^0$ channel 86
6.8 Comparison of the ϕ_h distribution for the data and the Monte Carlo simulation in the 3π channel 87
6.9 Comparison of the W distribution for the data and the Monte Carlo simulation 88

List of Tables

2.1 The two most sensitive observables for the measurement of the weak dipole moments . . . 10
2.2 Results on the weak dipole moments at 68 % C.L., from refs. [3, 4] . . . 12
2.3 Functions used in the original tau decay partial width . . . 14

4.1 Global τ selection efficiency . . . 39
4.2 Identification matrix for charged particles in tau decays . . . 41
4.3 Selection efficiencies for the channels of this analysis . . . 48
4.4 Number of reconstructed events for the decay combinations . . . 48
4.5 Data sample considered in this analysis . . . 49

6.1 Results of the fit of the*calibration curves* . . . 77
6.2 Results from the whole data sample, only with statistic error . . . 81
6.3 Correlation matrix between the fitted parameters . . . 81
6.4 Results from the whole data sample without any correction from the calibration curves . . . 82
6.5 Systematic uncertainties on $\Re(\mu_\tau)$ . . . 90
6.6 Systematic uncertainties on $\Im(\mu_\tau)$ . . . 90
6.7 Systematic uncertainties on $\Re(d_\tau)$ . . . 91
6.8 Systematic uncertainties on $\Im(d_\tau)$ . . . 91
6.9 Final results at 68 % C.L . . . 92
6.10 Comparison of this results with other measurements . . . 92
6.11 The 95% C.L. limits on the weak dipole moments . . . 93
6.12 The most sensitive observables for each of the tensorial couplings, showing if they are used for the first time in this analysis . . . 94

Chapter 1

Introduction

The modern theory describing the Electroweak and Strong Interactions, currently known as the Standard Model (SM) [1], was proposed by Glashow, Salam and Weinberg in the 60's. Very stringent tests of the theory have been done in present high energy colliders and, to date, all the experimental results agree with the SM predictions. Nevertheless, the theory is not complete and a few aspects remain not understood. For example, the CP–violation in the SM is not enough to explain the matter–antimatter ratio of the universe.

In the spirit of leaving no stone unturned, this thesis presents a measurement of the tensorial couplings of the τ lepton in $Z \to \tau^+\tau^-$ production at LEP. Due to gauge invariance, such couplings should be related with those from $\gamma \to \tau^+\tau^-$. Anyway, an experimental measurement is interesting to corroborate the expectations, and furthermore look for possible deviations from the SM.

To distinguish both types of tensorial couplings, the former are normally referred as Weak Dipole Moments (WDM) and the latter as Dipole Moments (DM). Within each of these two categories, one can also distinguish between the electric and the magnetic moments. The weak electric moment has the relevant feature of violating CP. It has been measured many times from the beginning of LEP. The set of published results on this coupling is given in refs. [2, 3, 4]. The weak magnetic moment has also been measured by the L3 [5] and the SLD [6] collaborations.

All these couplings are zero in the SM at first order. Nevertheless, the magnetic moments have non–vanishing contributions from quantum corrections, named anomalous magnetic moments. In 1948, the agreement of the experimental results

and the Schwinger's prediction for the anomalous magnetic moment of the electron [7] was a spectacular achievement of the quantum field theory. Nowadays, the experimental results on the magnetic moments are still relevant. An experiment is currently underway at Brookhaven to reduce the error on the anomalous magnetic moment of the muon by a factor of 20 [8].

The SM contribution from quantum corrections to the weak magnetic moment of the τ was calculated by Bernabéu et al. in ref. [9]. Such contribution turns out to be several orders of magnitude below the present experimental sensitivity. The SM contribution to the weak electric dipole moment is even smaller, as estimated in ref. [10]. Thus, any deviations from the expected values would be an indication of new physics, due to the small predictions of the modern theory.

This thesis uses the large data sample accumulated by the ALEPH detector from 1990 to 1995. The total integrated luminosity of the data is 155 pb^{-1}. The selection and particle identification are based on some algorithms previously developed in the ALEPH collaboration for tau data at LEP I. The new features of this analysis are mainly related with the use of all the cross–section terms in the extraction of the weak dipole moments.

The text is organised as follows. Chapter 2 presents the theoretical framework to understand the measurement of the weak dipole moments. Chapter 3 revises the performance of the ALEPH detector, with special emphasis on the more relevant subdetectors for this analysis. Chapter 4 describes the internal techniques of the ALEPH collaboration for tau analysis and other more general tools for any experiment running at the Z peak. Chapter 5 presents the main part of the method to extract the weak dipole moments. Chapter 6 covers the relevant systematic uncertainties and presents the final results of the analysis. Chapter 7 gives a summary and the conclusions. Finally, two appendixes explain more detail information on the analysis.

Chapter 2

Theoretical framework

This chapter covers the relevant theoretical concepts in tau physics to understand the measurement of the weak dipole moments.

The first part is focused on the $Z \to \tau^+\tau^-$ production. The Lorentz structure of this vertex is considered in detail. We present the total differential cross section used in the analysis and the most sensitive cross–section terms to the weak dipole moments.

Secondly, we consider the τ decay process, and give the formulae to access the spin information maximally.

2.1 Formalism for $Z \to \tau^+\tau^-$ production

The general Lorentz structure for the couplings of the Z boson to the τ leptons is explained below. In addition to the vector and axial vector couplings of the SM, other types of couplings [11] are allowed in a general approach.

2.1.1 Lorentz structure of $Z \to \tau^+\tau^-$

The general Lorentz structure for the process $e^+(k_1)e^-(k_2) \to \tau^+(p_1)\tau^-(p_2)$ can be described by the spin amplitude

$$M_{\lambda_1\lambda_2\alpha_1\alpha_2} = \sum_{(i)} g_{(i)}\bar{v}(k_1,\lambda_1)\Gamma_e^{(i)}u(k_2,\lambda_2)\cdot\bar{u}(p_2,\alpha_2)\Gamma_\tau^{(i)}v(p_1,\alpha_1)\,. \qquad (2.1)$$

The index $i = \gamma, Z$ refers to the photon and Z boson contributions. The quantities $\lambda_1, -\lambda_2, \alpha_1$ and $-\alpha_2$ are the helicities of the e^+, e^-, τ^+ and τ^-, respectively. The factors $g_{(i)}$ are the propagator functions, which depend on the center of mass energy $q = \sqrt{s}$. The terms $\Gamma_f^{(i)}$ are the currents. Finally, v and u are the Dirac spinors.

Besides γ and Z exchange, different types of exchange particles might appear: scalar (S), tensorial (T) or other types of vector contributions (V_{new}). The two former are expected to be too small to be measured at LEP, as discussed in ref. [11]. The V_{new} could be present, but they would appear first as a modification to the vector and axial vector couplings of γ and Z. Therefore, we concentrate on γ and Z exchange, but considering couplings more general than those of the SM.

The weak dipole moments are related with the electric dipole moments of the τ through gauge invariance, as mentioned in the introduction. Nevertheless, the γ exchange is very reduced with respect to that of the Z particle at an energy $\approx M_Z$. The suppression factor is of the order of $O(\Gamma_Z/M_Z)$. Therefore, we assume that the contribution from new physics may only come from the $Z\tau^+\tau^-$ vertex. The photon exchange is then described as in the SM, i.e.

$$\Gamma_f^{(\gamma)} = iQ_f e\gamma^\mu, \quad g_{(\gamma)} = 1/q^2, \tag{2.2}$$

where $Q_f e$ is the charge of the fermion, and $f = e, \tau$.

The general form of the current $\Gamma_f^{(Z)}$ for the Z exchange is

$$\Gamma_f^{(Z)} = ie\left[v_f\gamma^\mu - a_f\gamma^\mu\gamma_5 + i\frac{\mu_f}{\Lambda}\sigma^{\mu\nu}q_\nu + \frac{d_f}{\Lambda}\gamma_5\sigma^{\mu\nu}q_\nu - i\frac{s_f}{\Lambda}q^\mu + \frac{p_f}{\Lambda}\gamma_5 q^\mu\right], \tag{2.3}$$

with the propagator

$$g_{(Z)} = \frac{1}{q^2 - M_Z^2 + \Gamma q^2/M_Z}\,. \tag{2.4}$$

In these expressions, e is the electron charge, Λ is an arbitrary scale, (μ_f, d_f) are the weak dipole moments and (s_f, p_f) are the strengths for other possible scalar and pseudo-scalar couplings.

The vector and axial vector coupling v_f and a_f are given within $SU(2) \times U(1)$ by

$$v_f = x_f(I_3^f - 2Q_f s^2_{f,eff}), \;\; a_f = x_f I_3^f, \tag{2.5}$$

with

$$x_f = \sqrt{\frac{\sqrt{2}G_\mu M_Z^2 \rho_f}{e^2}} = \frac{\sqrt{\rho_f}}{2 s_{f,eff} c_{f,eff}}. \tag{2.6}$$

Within the SM, and in the Born approximation, $\rho_f = 1$, $s_{f,eff} = \sin\theta_W$, $c_{f,eff} = \cos\theta_W$, and θ_W is the weak mixing angle.

The couplings (s_f, p_f) of eq. 2.3 are parametrisations for possible contact terms in the Zf^+f^- vertex. They can be safely ignored for scattering at the Z pole, because of their vanishing value for a Z boson on shell [12]. Eq. 2.3 can then be re–written as

$$\Gamma_f^{(Z)} = ie\left[v_f\gamma^\mu - a_f\gamma^\mu\gamma_5 + i\frac{\mu_f}{\Lambda}\sigma^{\mu\nu}q_\nu + \frac{d_f}{\Lambda}\gamma_5\sigma^{\mu\nu}q_\nu\right] \; . \tag{2.7}$$

The subindex f stands either for e or τ. However, possible deviations from the SM are expected to appear in the $Z\tau^+\tau^-$ vertex first, since the τ mass is much larger than that of the e [13].

Thus, on the one hand, the Ze^+e^- vertex is described as in the SM, i.e.

$$\Gamma_e^{(Z)} = ie\left[v_e\gamma^\mu - a_e\gamma^\mu\gamma_5\right] \; . \tag{2.8}$$

On the other, the $Z\tau^+\tau^-$ vertex of eq. 2.7 is finally re-written as

$$\Gamma_\tau^{(Z)} = ie\left[v_\tau\gamma^\mu - a_\tau\gamma^\mu\gamma_5 + i\frac{\mu_\tau}{\Lambda}\sigma^{\mu\nu}q_\nu + \frac{d_\tau}{\Lambda}\gamma_5\sigma^{\mu\nu}q_\nu\right] \; . \tag{2.9}$$

In the above expressions, (μ_τ,d_τ) are the weak magnetic and the weak electric dipole moments of the τ. They are dimensionless quantities in the above equations. Λ is an arbitrary scale, which will be set to $2m_\tau$ through all this text. The electric moment is, however, mostly found in units of $e \cdot$ cm in the bibliography, by defining the contribution of this dipole moment to the current as $id_\tau\gamma_5\sigma^{\mu\nu}q_\nu$. These two different notations can be related with the conversion factor $\mathrm{e}/2m_\tau = 5.552 \times 10^{-15}\mathrm{e}\cdot\mathrm{cm}$.

2.1.2 Theoretical expectations within the SM

As mentioned in the introduction, the contribution to the magnetic moment from quantum corrections was determined in ref. [9]. The calculation is done at one loop radiative corrections within the SM and for the Z peak. The result is

$$\mu_\tau(M_Z^2) = -(2.10 + 0.61i) \times 10^{-6} \,. \tag{2.10}$$

The order of magnitude of the SM contribution for the weak electric dipole moment was estimated in ref. [10]. Several loop calculations have to be considered. The estimate of the typical amplitude is $10^{-7} \times T_{SM}$, with T_{SM} being the typical SM amplitude.

2.1.3 The Cross Section

From the spin amplitude of eq. 2.1 and with the γ and Z terms of equations (2.2, 2.8, 2.9), the differential cross section with unpolarised beams for $e^+e^- \to \tau^+\tau^-$ can be written as

$$\frac{d\sigma}{d\Omega}(\vec{s}_1, \vec{s}_2) \;=\; R_{00} + \sum_{i=1,\cdots,3} R_{i0}\, s_1^i + \sum_{j=1,\cdots,3} R_{0j}\, s_2^j + \sum_{i,j=1,\cdots,3} R_{ij}\, s_1^i s_2^j \,. \tag{2.11}$$

The R_{ij} terms are the spin matrix elements. They are a function of the fermion couplings to the Z (a_e, v_e, a_τ, v_τ, μ_τ, d_τ) and of the τ polar angle θ. The vectors ($\vec{s}_1$, $\vec{s}_2$) are the quantisation axes for the spin measurement of (τ^+, τ^-) in their corresponding rest frame.

In the previous equation, R_{00} is the total differential cross section, R_{i0} ($i = 1, \cdots, 3$) and R_{0j} ($j = 1, \cdots, 3$) are the polarisation along the directions of $\vec{s}_1$ and $\vec{s}_2$, and R_{ij} ($i, j = 1, \cdots, 3$) are the spin correlations between the two taus.

The above expression can also be written as

$$\frac{d\sigma}{d\Omega}(s_1, s_2) \;=\; \sum_{\mu,\nu=0,\cdots,3} R_{\mu\nu}\, s_1^\mu s_2^\nu \,, \tag{2.12}$$

with $s_1^0 = s_2^0 = 0$ in the tau rest frame.

The calculation of these matrix elements is simplified with the coordinate system of fig. 2.1. The z axis is along the τ^+ direction. The e^+ direction is in the $y-z$ plane. Hence, x is the component normal to the τ production plane and y is the transverse component.

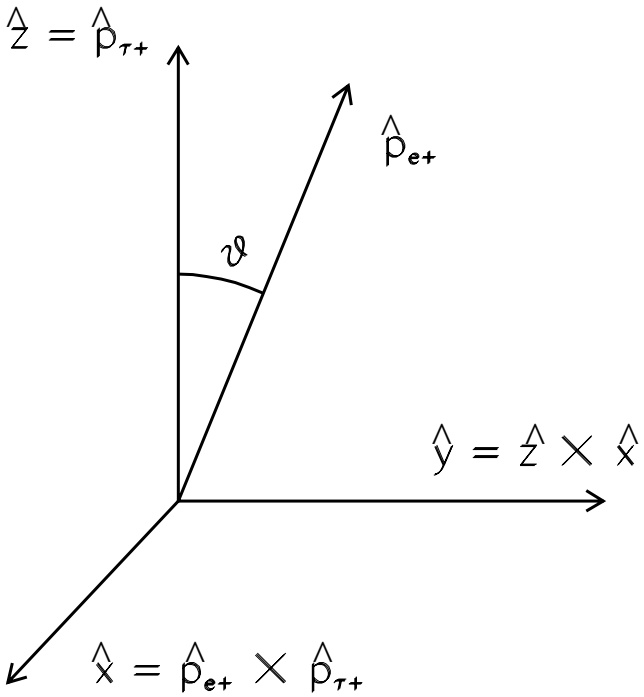

Figure 2.1: Coordinate system to describe $e^+e^- \to \tau^+\tau^-$ production.

Assuming this reference frame, the full explicit expression for R_{ij} $(i,j = 0,\cdots,3)$ is presented in appendix A. Both the Z and the γ contributions are included.

In the next section, we show the relationship between certain R_{ij} and common observables in tau physics at the Z peak, and present the most sensitive R_{ij} terms to the weak dipole moments.

Terms with only Standard Model couplings (SM) are given separately from those with weak dipole moments (ANM). The γ interchange is neglected in the following formulae for the sake of simplicity, although it is taken into account in the final numbers.

2.1.4 The cross section terms

R_{00} is the angular differential cross section. Its SM and ANM contributions are

$$\begin{aligned}
R_{00}|_{SM} &\propto (1+\cos^2\theta)(|a_e|^2+|v_e|^2)(|a_\tau|^2+|v_\tau|^2) \\
&+ 8\cos\theta\,\Re(v_e a_e{}^*)\Re(v_\tau a_\tau{}^*) + m^2\sin^2\theta\,|v_\tau|^2(|a_e|^2+|v_e|^2) \\
R_{00}|_{ANM} &\propto \frac{1}{m^2}\sin^2\theta\,(|a_e|^2+|v_e|^2)(|\mu_\tau|^2+|d_\tau|^2) \\
&+ 8\cos\theta\,\Re(v_e a_e{}^*)\Re(\mu_\tau a_\tau{}^*) + 4(|a_e|^2+|v_e|^2)\Re(v_\tau \mu_\tau{}^*) \\
&+ (1+\cos^2\theta)(|a_e|^2+|v_e|^2)|\mu_\tau|^2 \qquad (2.13)
\end{aligned}$$

Here, $m = m_\tau/(q/2)$, very small at the Z pole ($m \approx 0.039$).

A number of authors [14] have noted that the tau partial width of the Z already provides an upper limit on the weak dipole moments. Using the results on $\Gamma(Z \to \tau^+\tau^-)/\Gamma_0$ measured by the LEP and SLD collaborations [15], the upper bound is [1]

$$\sqrt{|\mu_\tau|^2+|d_\tau|^2} < 2.1\times 10^{-17} e\cdot cm \quad (95\%\ \text{C.L.})\,. \qquad (2.14)$$

The quadratic term in $R_{00}|_{ANM}$ is assumed to dominate over the linear terms.

The symmetric combination $(R_{03})_+ \equiv (R_{03}+R_{30})$ is related to the well known longitudinal polarisation, measured by the LEP collaborations [16]. The relation is

[1] This upper limit is 3.78×10^{-3} if both weak dipole moments are assumed dimensionless quantities.

$$P_z^+ = P_z^- = \frac{(R_{03})_+}{R_{00}}\,. \tag{2.15}$$

(We use the notation $(R_{ij})_+ \equiv (R_{ij} + R_{ji})$ and $(R_{ij})_- \equiv (R_{ij} - R_{ji})$ as of now.) The SM and ANM components of $(R_{03})_+$ are

$$\begin{aligned}
(R_{03})_+\Big|_{SM} &\propto (1+\cos^2\theta\,)(|a_e|^2+|v_e|^2)\Re(v_\tau {a_\tau}^*) \\
&+ 2\cos\theta\,(|a_\tau|^2+|v_\tau|^2)\Re(v_e {a_e}^*) \\
(R_{03})_+\Big|_{ANM} &\propto (1+\cos^2\theta\,)(|a_e|^2+|v_e|^2)\Re(\mu_\tau {a_\tau}^*) + 2\cos\theta\,\Re(v_e {a_e}^*)|\mu_\tau|^2 \\
&+ 4\cos\theta\,\Re(v_e {a_e}^*)\Re(\mu_\tau {v_\tau}^*)\,.
\end{aligned} \tag{2.16}$$

The sensitivity of the longitudinal polarisation to the weak magnetic dipole moment is very reduced. The ANM terms are of the same order as the SM terms for $\mu_\tau \approx 0.038$.

The diagonal elements (R_{22}, R_{11}) are proportional to the transverse-transverse and normal-normal spin correlations (P_{yy}^+, P_{xx}^+). The relation is

$$P_{yy}^+ = -P_{xx}^+ = \frac{R_{22}}{R_{00}} = -\frac{R_{11}}{R_{00}}\,. \tag{2.17}$$

The observables P_{yy}^+ and P_{xx}^+ have been measured by ALEPH and DELPHI [17]. The SM and ANM terms are in this case

$$\begin{aligned}
R_{22}|_{SM} &\propto \sin^2\theta\,(|a_e|^2+|v_e|^2)(|v_\tau|^2-|a_\tau|^2) \\
&+ m^2\sin^2\theta\,|v_\tau|^2(|a_e|^2+|v_e|^2) \\
R_{22}|_{ANM} &\propto \frac{1}{m^2}\sin^2\theta\,(|a_e|^2+|v_e|^2)(|\mu_\tau|^2-|d_\tau|^2) \\
&+ 4\sin^2\theta\,(|a_e|^2+|v_e|^2)\Re(v_\tau {\mu_\tau}^*) + \sin^2\theta\,(|a_e|^2+|v_e|^2)|\mu_\tau|^2\,.
\end{aligned} \tag{2.18}$$

The transverse-normal spin correlation,

$$P_{yz}^+ = \frac{(R_{21})_+}{R_{00}}\,, \tag{2.19}$$

has also been measured in the previous references. The corresponding SM and ANM components are

$$\begin{aligned} (R_{21})_+\Big|_{SM} &\propto \sin^2\theta\,(|a_e|^2+|v_e|^2)\Im(v_\tau a_\tau{}^*) \\ (R_{21})_+\Big|_{ANM} &\propto \sin^2\theta\,(|a_e|^2+|v_e|^2)\Im(\mu_\tau a_\tau{}^*)\,. \end{aligned} \tag{2.20}$$

A limit on $\Im(\mu_\tau)$ was obtained in ref. [18] from the ALEPH measurement of the transverse-normal spin correlations. This bound is

$$\Im(\mu_\tau) \;<\; 0.04 \quad (\text{at } 68\ \%\ \text{C.L.})\,. \tag{2.21}$$

Now, we move to observables related to the weak dipole moments. The two most sensitive observables to each of the weak dipole moments are given in table 2.1. The observables $(A_{ij})_{+/-}$ are defined as

$$(A_{ij})_{+/-} \equiv \frac{(R_{ij})_{+/-}}{R_{00}}\,. \tag{2.22}$$

The corresponding $(R_{ij})_{+/-}$ terms are given at length for each of the anomalous couplings. We separate the SM and ANM contributions as done before.

$\Re(\mu_\tau)$		$\Im(\mu_\tau)$		$\Re(d_\tau)$		$\Im(d_\tau)$	
$1st.Obs.$	$2nd.Obs.$	$1st.Obs.$	$2nd.Obs.$	$1st.Obs.$	$2nd.Obs.$	$1st.Obs.$	$2nd.Obs.$
$(A_{02})_+$	$(A_{32})_+$	$(A_{31})_+$	$(A_{01})_+$	$(A_{01})_-$	$(A_{31})_-$	$(A_{32})_-$	$(A_{02})_-$

Table 2.1: The two most sensitive observables for the measurement of the weak dipole moments.

For $\Re(\mu_\tau)$:

$$\begin{aligned} (R_{02})_+\Big|_{SM} &\propto 2m\sin\theta\,|v_\tau|^2\Re(v_e a_e{}^*) + m\sin\theta\,\cos\theta\,(|a_e|^2+|v_e|^2)\Re(v_\tau a_\tau{}^*) \\ (R_{02})_+\Big|_{ANM} &\propto \frac{1}{m}\sin\theta\,\cos\theta\,(|a_e|^2+|v_e|^2)\Re(a_\tau\mu_\tau{}^*) \\ &+ \frac{2}{m}\sin\theta\,\Re(v_e a_e{}^*)\Re(v_\tau\mu_\tau{}^*) + 2m\sin\theta\,\Re(v_e a_e{}^*)\Re(v_\tau\mu_\tau{}^*) \\ &+ \frac{2}{m}\sin\theta\,\Re(v_e a_e{}^*)|\mu_\tau|^2 \end{aligned} \tag{2.23}$$

$$
\begin{aligned}
(R_{32})_+\Big|_{SM} &\propto 2m\sin\theta\,\Re(v_e a_e{}^*)\Re(v_\tau a_\tau{}^*) + m\sin\theta\,\cos\theta\,(|a_e|^2+|v_e|^2)|v_\tau|^2 \\
(R_{32})_+\Big|_{ANM} &\propto \frac{1}{m}\sin\theta\,\cos\theta\,(|a_e|^2+|v_e|^2)\Re(v_\tau\mu_\tau{}^*) \\
&+ \frac{2}{m}\sin\theta\,\Re(v_e a_e{}^*)\Re(a_\tau\mu_\tau{}^*) + m\sin\theta\,\cos\theta\,(|a_e|^2+|v_e|^2)\Re(v_\tau\mu_\tau{}^*) \\
&+ \sin\theta\,\cos\theta\,(|a_e|^2+|v_e|^2)|\mu_\tau|^2 \qquad (2.24)
\end{aligned}
$$

For $\Im(\mu_\tau)$:

$$
\begin{aligned}
(R_{31})_+\Big|_{SM} &\propto m\sin\theta\,\cos\theta\,(|a_e|^2+|v_e|^2)\Im(v_\tau{}^* a_\tau) \\
(R_{31})_+\Big|_{ANM} &\propto \frac{1}{m}\sin\theta\,\cos\theta\,(|a_e|^2+|v_e|^2)\Im(a_\tau\mu_\tau{}^*) + \frac{2}{m}\sin\theta\,\Re(v_e a_e{}^*)\Im(v_\tau\mu_\tau{}^*) \\
&+ 2m\sin\theta\,\Re(v_e a_e{}^*)\Im(v_\tau{}^*\mu_\tau) \qquad (2.25)
\end{aligned}
$$

$$
\begin{aligned}
(R_{01})_+\Big|_{SM} &\propto 2m\sin\theta\,\Re(v_e a_e{}^*)\Im(v_\tau{}^* a_\tau) \\
(R_{01})_+\Big|_{ANM} &\propto \frac{1}{m}\sin\theta\,\cos\theta\,(|a_e|^2+|v_e|^2)\Im(v_\tau\mu_\tau{}^*) + \frac{2}{m}\sin\theta\,\Re(v_e a_e{}^*)\Im(a_\tau\mu_\tau{}^*) \\
&+ m\sin\theta\,\cos\theta\,(|a_e|^2-|v_e|^2)\Im(v_\tau{}^*\mu_\tau) \qquad (2.26)
\end{aligned}
$$

For $\Re(d_\tau)$:

$$
\begin{aligned}
(R_{01})_-\Big|_{SM} &\propto 0 \\
(R_{01})_-\Big|_{ANM} &\propto -\frac{1}{m}\sin\theta\,\cos\theta\,(|a_e|^2+|v_e|^2)\Re(a_\tau d_\tau{}^*) - \frac{2}{m}\sin\theta\,\cos\theta\,\Re(v_e a_e{}^*)\Re(v_\tau d_\tau{}^*) \\
&- \frac{2}{m}\sin\theta\,\Re(v_e a_e{}^*)\Re(\mu_\tau d_\tau{}^*) \qquad (2.27)
\end{aligned}
$$

$$
\begin{aligned}
(R_{31})_-\Big|_{SM} &\propto 0 \\
(R_{31})_-\Big|_{ANM} &\propto -\frac{1}{m}\sin\theta\,\cos\theta\,(|a_e|^2+|v_e|^2)\Re(v_\tau d_\tau{}^*) - \frac{2}{m}\sin\theta\,\Re(v_e a_e{}^*)\Re(a_\tau d_\tau{}^*) \\
&- \frac{1}{m}\sin\theta\,\cos\theta\,(|a_e|^2+|v_e|^2)\Re(\mu_\tau d_\tau{}^*) \qquad (2.28)
\end{aligned}
$$

For $\Im(d_\tau)$:

$$\begin{aligned}
(R_{32})_-\Big|_{SM} &\propto 0 \\
(R_{32})_-\Big|_{ANM} &\propto -\frac{1}{m}\sin\theta\,\cos\theta\,(|a_e|^2+|v_e|^2)\Im(a_\tau {d_\tau}^*) - \frac{2}{m}\sin\theta\,\Re(v_e {a_e}^*)\Im(v_\tau {d_\tau}^*) \\
&- \frac{2}{m}\sin\theta\,\Re(v_e {a_e}^*)\Im(\mu_\tau {d_\tau}^*) \qquad (2.29)
\end{aligned}$$

$$\begin{aligned}
(R_{02})_-\Big|_{SM} &\propto 0 \\
(R_{02})_-\Big|_{ANM} &\propto -\frac{1}{m}\sin\theta\,\cos\theta\,(|a_e|^2+|v_e|^2)\Im(v_\tau {d_\tau}^*) - \frac{2}{m}\sin\theta\,\Re(v_e {a_e}^*)\Im(a_\tau {d_\tau}^*) \\
&- \frac{1}{m}\sin\theta\,\cos\theta\,(|a_e|^2+|v_e|^2)\Im(\mu_\tau {d_\tau}^*) \qquad (2.30)
\end{aligned}$$

Assuming universality, the biggest factors multiplying the anomalous couplings for the first and the second most sensitive observables are $a^3/m \approx 3.21$ and $a^2 v/m \approx 0.25$, respectively.

The most sensitive terms to $\Re(d_\tau)$ and $\Im(d_\tau)$ have been used in previous measurements [2]. The most sensitive observable to $\Re(\mu_\tau)$ and the second most sensitive observable to $\Im(\mu_\tau)$ have been measured by L3 [5], as suggested in ref. [9]. We summarize the current results on the weak dipole moments in table 2.2. The numbers are extracted from refs. [3, 4].

Exper.	$\Re(\mu_\tau)[10^{-3}]$	$\Im(\mu_\tau)[10^{-3}]$	$\Re(d_\tau)[10^{-18}\mathrm{e}\cdot\mathrm{cm}]$	$\Im(d_\tau)[10^{-18}\mathrm{e}\cdot\mathrm{cm}]$
L3	$0.0 \pm 1.6 \pm 2.3$	$-1.0 \pm 3.6 \pm 4.3$	$-4.4 \pm 8.8 \pm 13.3$	-
SLD	$0.26 \pm 0.99 \pm 0.75$	$-0.02 \pm 0.62 \pm 0.24$	$1.8 \pm 6.1 \pm 2.8$	$-2.6 \pm 3.5 \pm 1.3$
ALEPH	-	-	$-0.29 \pm 2.59 \pm 0.88$	-
OPAL	-	-	$0.72 \pm 2.46 \pm 0.24$	$3.5 \pm 5.7 \pm 0.8$
DELPHI	-	-	$-1.48 \pm 2.64 \pm 0.27$	$-4.4 \pm 7.7 \pm 1.3$

Table 2.2: Results on the weak dipole moments at 68 % C.L. extracted from refs. [3, 4]. The errors are splitted in their statistical and systematic components.

In this analysis we use, for the first time, the most sensitive observable to $\Im(\mu_\tau)$, i.e. $(A_{31})_+$. This was suggested in ref. [19]. We also use the remaining set of observables shown before, together with the information coming from all the spin density matrix elements. We conduct this with a log–likelihood fit, explained in section 2.3 of this chapter and in chapter 5.

2.2 Tau decay

The calculation of most of the partial and total decay rates of the tau were done by Tsai in 1971 [20], before the tau discovery. For the $\pi\nu_\tau$ decay used in this analysis, Tsai's expressions are used. Nevertheless, for the rest of decays, resonances were not taken into account in the pioneering work of Tsai, but they are included in the more recent work on tau decays, TAUOLA [21]. Thus, we use the TAUOLA formulae for those decays.

In the original calculation, the differential partial rate of the tau decay into one charged particle,

$$\tau^{\pm}(q) \to f^{\pm}(p_f) + \text{neutrals},$$

read as follows (in the τ rest frame) [22]

$$\frac{d\Gamma(\tau^{\mp})}{d\Omega dx} = \frac{1}{4\pi} a(x)(1 \pm g(x)\vec{n}\cdot\vec{s}) \,, \tag{2.31}$$

where $x = E_f/m_\tau$, $\vec{n} = \vec{p}_f/|\vec{p}_f|$ and $\vec{s}$ is the τ polarisation vector in its rest frame.

The functions $a(x)$ and $g(x)$ are listed in table 2.3 for $f = \pi$, ρ and a_1. The $g(x)$ is a constant in the three cases shown and is called the analysing power of the decay mode. For the scalar particle π, it is equal to 1, and it is smaller for the vector particles ρ and a_1. For the two latter, the existence of helicity 1 states reduces the sensitivity to the tau polarisation and this is, furthermore, a function of the hadron mass.

This analysis has about 50% of events with at least one identified a_1 decay mode, where the loss of sensitivity would be 98% using the above formula. However, the sensitivity can be recovered by measuring the helicity of the hadronic system, following the ideas developed for the TAUOLA Monte Carlo program.

Hence, for the decay of a polarised tau,

$$\tau^{-}(q,s) \to \nu_\tau(k_1)\, x_2(k_2)\, x_3(k_3)\, \cdots\, x_n(k_n) \,,$$

we express the differential partial width in the tau rest frame as in the TAUOLA paper [21],

$$d\Gamma(s) = \frac{1}{2m_\tau} |\bar{M}|^2 (1 - h_\mu s^\mu) d\mathrm{PS}(q; k_1, k_2, \cdots, k_n) \,, \tag{2.32}$$

where s^μ is the polarisation vector of the tau; h^μ is the polarimeter vector, a function of q and k_i, and different for each of the decay channels; dPS is the Lorentz invariant phase space,

$$d\mathrm{PS}(q; k_1, k_2, \cdots, k_n) = (2\pi)^4 \delta^4(q - \sum_{i=1}^{n} k_i) \prod_{i=1}^{n} \frac{d^3 k_i}{(2\pi)^3 2k_i^0} ,$$

and $|\bar{M}|^2$ is the spin averaged squared matrix element.

Decay mode	$a(x)$	$g(x)$	Comments
$\tau^- \to \pi^- \nu_\tau$	$\delta(1-x)$	1	
$\tau^- \to \rho^- \nu_\tau$	$\delta(1+\rho^2-x)$	$\frac{1-2\rho^2}{1+2\rho^2} = 0.45$	$\rho^2 = \left(\frac{m_\rho}{m_\tau}\right)^2 = 0.187$
$\tau^- \to a_1^- \nu_\tau$	$\delta(1+\rho^2-x)$	$\frac{1-2\rho^2}{1+2\rho^2} = 0.02$	$\rho^2 = \left(\frac{m_{a_1}}{m_\tau}\right)^2 = 0.479$

Table 2.3: Functions $a(x)$ and $g(x)$ defined in eq. 2.31. The particle masses are taken from ref. [23].

The phase space dPS is parametrized as in ref. [24],

$$d\mathrm{PS}(q; k_1, k_2, \cdots, k_n) = P \, \mathrm{d}\bar{X} , \tag{2.33}$$

where P is a phase space factor depending on the number of final state particles and on the presence of possible resonances, and $\bar{X}$ is a set of independent variables (the kinematical variables of the tau decay products used to infer its polarisation). The expressions of P and $\bar{X}$ are presented in appendix B for each of the tau decay modes considered.

The zeroth component of the h_μ vector can be defined arbitrarily and we choose it to be zero as in ref. [21]. $d\Gamma(s)$ is then expressed as

$$d\Gamma(\vec{s}) = \frac{1}{2m_\tau} |\bar{M}|^2 (1 + \vec{h} \cdot \vec{s}) P \, \mathrm{d}\bar{X} . \tag{2.34}$$

For the decay of an unpolarised tau, the above expression is reduced to

$$d\Gamma = \frac{1}{2m_\tau} |\bar{M}|^2 P \, \mathrm{d}\bar{X} . \tag{2.35}$$

In eq. 2.34, the decay dependent elements, in general functions of the decay particles momenta, are $\vec{h}$, $|\bar{M}|^2$ and P; their explicit expressions are extracted from

the TAUOLA paper and are given in appendix B. The decay to one pion is the simplest; in this case, $|\bar{M}|^2$ is a constant and $\vec{h}$ is proportional to the pion momentum in the tau rest frame.

For a decay mode i, we will use in the following section the fact that the integration of eq. 2.35 over the whole final phase space is the partial width Γ_i of the decay channel considered,

$$\Gamma_i = \frac{1}{2m_\tau} \int |\bar{M}|^2 P \, \mathrm{d}\bar{X} \; . \tag{2.36}$$

2.3 Final combined cross section and likelihood fitting

The differential cross section for $e^+e^- \to \tau^+\tau^-$ with unpolarised beams has been presented in section 2.1.3. It can also be expressed as,

$$d\sigma(s_1, s_2) = |A|^2(1 + a_\mu s_1^\mu + b_\mu s_2^\mu + c_{\mu\nu} s_1^\mu s_2^\nu)\, d\Omega \; , \tag{2.37}$$

where $|A|^2 \equiv R_{00}$, $a_\mu \equiv R_{\mu 0}/R_{00}$, $b_\mu \equiv R_{0\mu}/R_{00}$ and $c_{\mu\nu} \equiv R_{\mu\nu}/R_{00}$. Sum over repeated indexes is assumed from now on.

For the whole process,

$$\begin{aligned} e^+(p_1) + e^-(p_2) \to \quad & \tau^+(q_1) \quad + \tau^-(q_2) \\ & \tau^+(q_1) \quad \to \bar{\nu}_\tau(k_1)\, x_2(k_2) \cdots x_n(k_n) \\ & \tau^-(q_2) \quad \to \nu_\tau(k_1')\, x_2'(k_2') \cdots x_{n'}'(k_{n'}') \; , \end{aligned}$$

the differential cross section was first derived by Tsai. Formal demonstrations can be found in [25, 22]. In ref. [25] it is shown that in the assumptions of $\Gamma_\tau \ll m_\tau$ (which is always true), on–shell τ's (which is verified at LEP energies) and for a decay topology of the taus (ij), the differential cross section of the whole process is

$$(d\sigma_T)_{ij} = 4\, d\sigma(h_1, h_2) \times \frac{d\Gamma_i}{\Gamma} \times \frac{d\Gamma_j}{\Gamma} \; , \tag{2.38}$$

where $d\sigma(h_1, h_2)$ is equal to eq. 2.37, with the substitution of $(s_1,\, s_2)$ by $(h_1,\, h_2)$; $d\Gamma_i$ is the differential partial width of channel i for an unpolarised tau (which was written in eq. 2.35), and Γ is the total tau width.

Turning back to the notation of eq. 2.12, we can write the differential cross section in the following way:

$$(d\sigma_T)_{ij} \propto R_{\mu\nu}\, H_i^{\mu}\, H_j^{\nu}\, d\,\Omega d\bar{\mathrm{X}}_1 d\bar{\mathrm{X}}_2\ , \tag{2.39}$$

where the $R_{\mu\nu}$ terms were introduced in section 2.1.3, $(\bar{\mathrm{X}}_1,\ \bar{\mathrm{X}}_2)$ are the set of independent variables to infer the polarisation of the $(\tau^+,\ \tau^-)$, and H^{μ} are related with the previous h^{μ} as follows,

$$H^{\mu} = W h^{\mu} \qquad \text{with} \qquad W \equiv \frac{|\bar{M}|^2}{2m_\tau}\, P\,. \tag{2.40}$$

We have taken $h^0 = 1$ to unify the notation. $|\bar{M}|^2$ was introduced in the previous section as the spin average squared matrix element for a given tau decay. W is a kinematical variable which can be measured for each tau decay using the equations presented in appendix B.

In this context, the dependence on the anomalous couplings $(\mu_\tau,\ d_\tau)$ and on the measurable variables $(\Omega,\ W_1,\ \cos\theta_{h_1},\ \phi_{h_1},\ W_2,\ \cos\theta_{h_2},\ \phi_{h_2})$ is

$$\begin{aligned} R_{\mu\nu} &= R_{\mu\nu}(\mu_\tau, d_\tau, \Omega)\ , \\ H_i^{\mu} &= H_i^{\mu}(W_1, \cos\theta_{h_1}, \phi_{h_1}) \text{ and} \\ H_j^{\nu} &= H_j^{\nu}(W_2, \cos\theta_{h_2}, \phi_{h_2})\ , \end{aligned}$$

where the $(\theta_{h_1},\ \theta_{h_2},\ \phi_{h_1},\ \phi_{h_2})$ are the polar and the azimuthal angles of $\vec{h}_1$ and $\vec{h}_2$, which are calculated in the reference frame of fig. 2.1.

In order to calculate the likelihood for an observed event with decay topology ij, we start by obtaining the $(H_i,\ H_j)$ using eq. 2.40. For $(W_1,\ \cos\theta_{h_1},\ \phi_{h_1},\ W_2,\ \cos\theta_{h_2},\ \phi_{h_2})$ we use the expressions of appendix B. The likelihood is then a function of the anomalous couplings (μ_τ, d_τ) for given values of $(\Omega,\ W_1,\ \cos\theta_{h_1},\ \phi_{h_1},\ W_2,\ \cos\theta_{h_2},\ \phi_{h_2})$. In terms of the more compact differential cross section, the likelihood for an event with decay topology (ij) is

$$\begin{aligned} &L_{ij}(\mu_\tau, d_\tau |\, \Omega, W_1, \cos\theta_{h_1}, \phi_{h_1}, W_2, \cos\theta_{h_2}, \phi_{h_2}) = \\ &\bar{N}\, R_{\mu\nu}(\mu_\tau, d_\tau, \Omega) H_i^{\mu}(W_1, \cos\theta_{h_1}, \phi_{h_1}) H_j^{\nu}(W_2, \cos\theta_{h_2}, \phi_{h_2})\ , \end{aligned} \tag{2.41}$$

where $\bar{N}$ is the normalization factor of the likelihood, such that the integration over all possible decay parameters $(\bar{X}_1,\ \bar{X}_2)$ and all possible decay topologies is

$$\sum_{ij} \int L_{ij}(\mu_\tau, d_\tau|\Omega, W_1, \cos\theta_{h_1}, \phi_{h_1}, W_2, \cos\theta_{h_2}, \phi_{h_2}) d\bar{X}_1 d\bar{X}_2 = 1 \; . \tag{2.42}$$

Hence,

$$\bar{N}(\mu_\tau, d_\tau, \Omega) = \frac{1}{|A|^2(\mu_\tau, d_\tau, \Omega)} \; . \tag{2.43}$$

In order to conveniently absorb the normalization terms, we finally write the likelihood as,

$$\begin{aligned} &L_{ij}(\mu_\tau, d_\tau|\, \Omega, W_1, \cos\theta_{h_1}, \phi_{h_1}, W_2, \cos\theta_{h_2}, \phi_{h_2}) = \\ &\bar{R}_{\mu\nu}(\mu_\tau, d_\tau, \Omega) \bar{H}_i^\mu(W_1, \cos\theta_{h_1}, \phi_{h_1}) \bar{H}_j^\nu(W_2, \cos\theta_{h_2}, \phi_{h_2}) \; , \end{aligned} \tag{2.44}$$

with the following definitions:

$$\begin{aligned} \bar{R}_{\mu\nu}(\mu_\tau, d_\tau, \Omega) &\equiv \frac{R_{\mu\nu}(\mu_\tau, d_\tau, \Omega)}{|A|^2(\mu_\tau, d_\tau, \Omega)} \\ \bar{H}^\mu(W, \cos\theta_h, \phi_h) &\equiv \frac{W h^\mu}{\Gamma_\tau} \; . \end{aligned}$$

Normalized in this fashion, the likelihood of the observed data only depends upon the net spin polarisation of the produced tau pairs, and not upon the total rate of tau production as a function of the $\cos\theta$ angle.

If we included the integral over Ω in eq. 2.42, we would also use the information of R_{00} on the anomalous couplings. However, we showed in section 2.1.4 that the dependence of R_{00} on the anomalous terms is very weak, and, moreover, quadratic. Hence, small differences between the observed and expected event rate as a function of $\cos\theta$ would produce very large values of the anomalous couplings.

Therefore, we have normalized the likelihood as shown in eq. 2.42.

Chapter 3

Description of the experiment

The measurement of the tau weak dipole moments conducted in this thesis is based on the data taken with the ALEPH detector at LEP I ($\sqrt{s} \approx M_Z \approx 91.19$ GeV/c^2).

In the first section of this chapter, a brief description of the LEP collider is presented. The ALEPH detector is explained after, with special attention to the relevant parts for the analysis. Finally, two sections are devoted to the trigger of the detector and to the data acquisition system and the event reconstruction procedure.

3.1 The LEP collider

The LEP collider (Large Electron Positron collider) [26] is a historic e^+e^- machine which was closed on the 2nd of November of the year 2000 to start with the LHC program. It was a very successful project, in which very detailed measurements were performed.

It had a total circumference of 27 Km and was sited at CERN (Centre Européene pour la Reserche Nucléaire) in Geneva. Electrons and positrons were continuously traversing the Swiss and French borders in an underground tunnel with depth varying from 80 to 140 m (see fig. 3.1).

The original project was conceived as two operational stages. The first one, called LEP I, started in 1989 and extended up to 1995. The beam center of mass energy was $\approx M_Z$ and very detailed electroweak studies of the Z boson were carried out. The second phase, LEP II, was in operation since 1996 up to the year 2000.

The center of mass energy was highered up to $\approx$ 200 GeV to study the properties of the W pairs produced and search for possible new physics.

The beams of electrons and positrons consisted of either four or eight bunches, and could collide in eight or sixteen points in principle. However, they were steered to only cross in the four LEP experiments (ALEPH, DELPHI, OPAL and L3) every 23 or 12 μs. A system of electrostatic separators avoided the other collisions.

The LEP machine was built up of eight arcs alternating with eight straight sections. In four of these straight sections the experiments were located. Dipole magnets bent the trajectory of the beams in the arcs, and a combination of quadrupoles produced a strong focusing effect in the straight sections increasing the machine luminosity.

The initial LEP configuration was four bunches of electrons and positrons (4x4) separated 23 μs. From October 1992 up to 1994 a new configuration of (8x8) bunches was adopted. The typical luminosities achieved in this phase were $1 - 2 \times 10^{31}\mathrm{cm}^{-2}\mathrm{s}^{-1}$. In 1995, LEP went back to the previous scheme of (4x4), but each bunch was divided in two. The latter was in principle the configuration foreseen for LEP II in order to achieve the desirable expected luminosity of $10^{32}\mathrm{cm}^{-2}\mathrm{s}^{-1}$.

The acceleration of the beam was performed by old room temperature copper Radio Frequency (RF) cavities at LEP I, which were partially replaced by new niobium super-conducting RF for the second stage. These cavities accelerated the beam to the desired energy, and also compensated for the loss due to synchrotron radiation, very important for electrons and positrons at the typical LEP energies. The mean value of this energy loss per turn is proportional to E^4/m^4R, where E is the particle energy, m is the mass and R is the radius of curvature.

The LEP injection chain can be seen schematically in fig. 3.2. It will have certainly some common features with that of the LHC, because the idea is to use previous accelerators built at CERN. The whole chain for the LEP period could be divided in two phases, explained in the two following paragraphs. The accelerating machines were linear colliders in the first stage, and circular rings in the second stage.

In the first phase, electrons and positrons were accelerated in two stages in the LInear Lep injector (LIL injector). First, electrons were accelerated up to 200 MeV in a LINear ACcelerator (LINAC). A fraction of them was then used to collide with

a fix target of tungsten producing positrons. Secondly, both electrons and positrons were accelerated in a second LINAC up to 600 MeV.

In the second phase, both electrons and positrons entered a set of circular machines, as said before. They first encountered a small Electron Positron Accumulator (EPA), where particles were separated into bunches, and stored circulating until an intensity of $\approx 10^{10}$ particles per bunch was achieved. When this intensity was achieved, the bunches were injected into the CERN Proton Synchrotron (PS), being accelerated up to 3.5 GeV. The next step was the CERN Super Proton Synchrotron (SPS), where the energy achieved was 20 GeV. Finally, the beams were injected into the LEP storage ring to be accelerated up to the desired final energy.

The circumferences of the EPA, PS and SPS are 0.12 Km, 0.6 Km, and 7 Km, respectively.

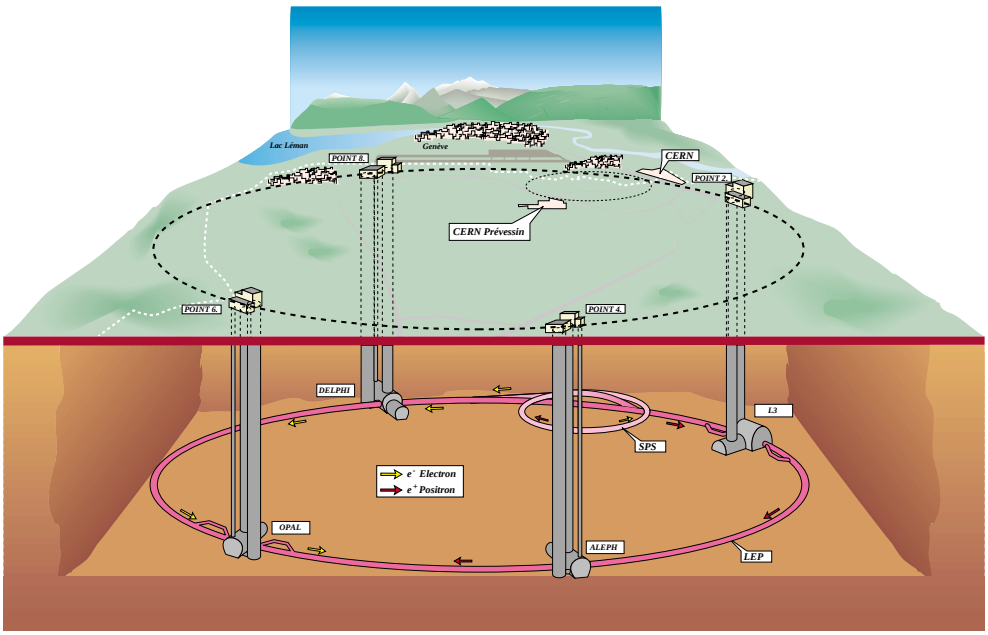

Figure 3.1: View of the LEP ring and the four interaction points.

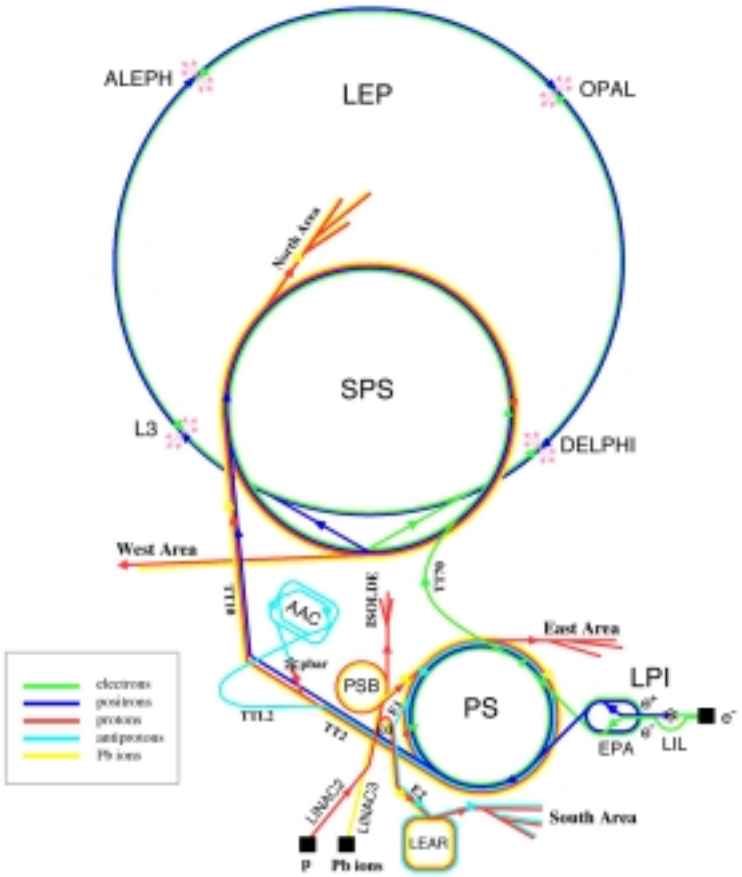

Figure 3.2: The LEP acceleration chain.

3.2 The ALEPH detector

ALEPH [27, 28] was one of the four LEP experiments, located in the interaction point number four. A general view of the experiment can be seen in fig. 3.3. The detector was placed in an underground cavern with a depth of 143 m, very close to the Jura mountains. It was cylindrical, with a diameter of 12 m and a length of 12 m. The total weight was about 4000 tons. The positive z coordinate was along the electron direction (see fig. 3.1), but it was not completely horizontal because of the slight tilt of the machine. The x coordinate was pointing towards the centre of the accelerator and y was defined by being orthogonal to x and z.

In the whole structure, specialised subdetectors could be distinguished. One set of these subdetectors, very relevant for this analysis, were the tracking devices: Vertex DETector (VDET) [29], Inner Tracking Chamber (ITC) [30] and Time Projection Chamber (TPC) [31]. These devices allowed to determine the direction of charged particles, their momentum and also provided particle identification through ionisation energy loss. A second set of subdetectors, also very important in this measurement, were the calorimeters: Electromagnetic CALorimeter (ECAL) and Hadron CALorimeter (HCAL). In general, calorimeters are the only subdetectors able to measure the energy and direction of the neutral particles, and also provide energy measurements for charged hadrons. Apart from these two sets of detectors, the Super-conducting Magnet Coil was around ECAL, giving an axial magnetic field in the tracking system of 1.5 T. The Muon Chambers were surrounding HCAL to provide muon identification. Finally, two more sets of subdetectors completed the experiment: the luminosity detectors and the beam and background monitors.

The tracking devices and the calorimeters are explained in detail in the following subsections. For the luminosity detectors and the beam and background monitors a few words are said at length.

The luminosity measurement is very important for analysis which measure physical cross–sections but it is not essential in this thesis. We had three subdetectors in ALEPH specialised in luminosity measurements: Luminosity CALorimeter (LCAL), SIlicon luminosity CALorimeter (SICAL) [32] and Bhabha CALorimeter (BCAL) [33]. All of them identified Bhabha events mainly as coincidences of back–to–back energy depositions. The luminosity was obtained dividing the total number of events by the theoretical expected cross–section, calculated with very high precision for Bhabha events at the Z peak.

The LCAL subdetector was very similar to ECAL, explained with more detail later. It was a sampling calorimeter made of alternating lead sheets and proportional wire chambers. Two pairs of semi–circular modules were placed around the beam pipe, at each end of the detector, and the total acceptance was from 38.4 to 195 mrad (in polar angle). At the beginning of LEP I operation, it was the official ALEPH detector for luminosity measurement and, also, in the whole LEP II phase. In September 1992, SICAL was installed and replaced LCAL until 1995 as official luminosity subdetector due to its better performance.

SICAL alternated tungsten sheets with 12 silicon layers for the readout of energy and position measurements. The total acceptance was from 27.9 to 62.7 mrad at LEP I. However, it was considerably reduced at LEP II, due to the mask for protecting the rest of ALEPH subdetectors from the higher synchrotron radiation at higher energies. This mask caused the luminosity performance of LCAL to be better than that of SICAL at LEP II, but anyway the role of SICAL at LEP II was very important in the event reconstruction at low angle.

BCAL was a very low angle subdetector, sited at 7.1 m from the interaction point giving an on–line monitoring of the luminosity. It was made of tungsten converter sheets sandwiched with sampling layers of plastic scintillators. A plane of silicon strips with $r\phi$ segmentation allowed to locate the shower position. The angular acceptance was from 5.1 to 9 mrad. From 1997 up to the end of LEP, a new BCAL was installed with PMT and APD readout for the plastic scintillators. The luminosity performance was improved and the new monitor was also used in the 2-γ trigger of ALEPH.

The background conditions in ALEPH and the beam performance of LEP were monitored by two more subdetector: the Small Angle Monitor of BAckground (SAMBA) and the Beam Orbit Monitors (BOMs).

SAMBA was located in front of LCAL at either end of the detector. On each side, two multiwire proportional chambers were sited with readout in two rings of eight pads per ring.

The BOMs were devices placed around the beam pipe to determine the position of escaping particles. They also were used by the LEP operators to optimise the beam conditions, and by ALEPH to determine the coordinates of the beam spot in the interaction point.

3.2.1 VDET

The VDET was fully operational since the start of the 1991 running period, and was replaced by a new, improved version (VDET II) in the late summer of 1995, for the LEP II phase. We will only consider here the VDET version operational with LEP I data. The configuration of this device can be seen in fig. 3.4. It was formed by two cylindrical layers: one at 6.3 cm from the interaction point and the

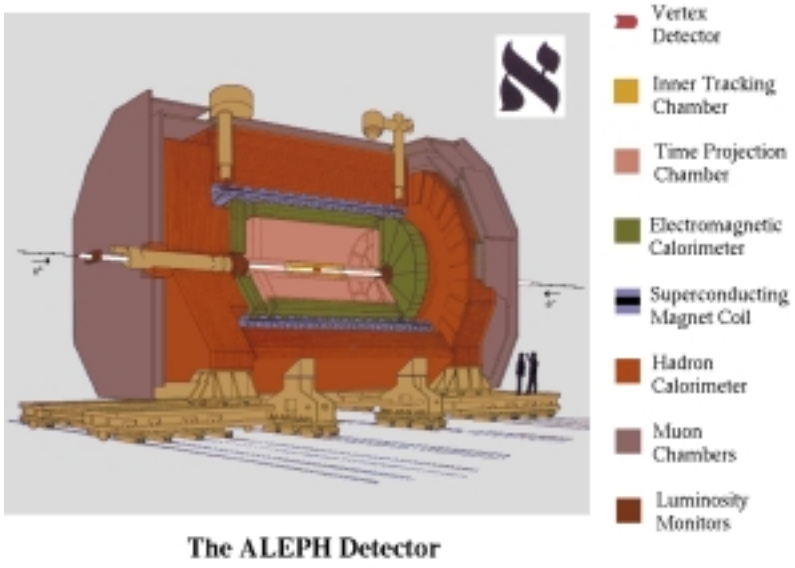

Figure 3.3: The ALEPH detector.

other at 11.0 cm. Both layers had double sided silicon strips with z readout in the inner part and $r\phi$ readout in the outer part. The coordinate spatial resolution was 10 μm for z and 12 μm for $r\phi$.

The role of the VDET was fundamental in the reconstruction of particles with very short life–times, like hadrons with b and c quarks, and for the τ lepton, through the determination of the impact parameters of its decay products. It was also very important in the reconstruction of charged tracks starting with TPC and ITC hits and extrapolating to VDET with two very precise hits.

3.2.2 ITC

The ITC was a cylindrical multiwire drift chamber, filled with a mixture of $Ar(50\ \%)$ and $C_2H_6(50\ \%)$. It was 2 m long. The inner radius was 12.8 cm, and the outer radius was 28.8 cm. An overall view of this chamber is presented in fig. 3.5, before its insertion in the ALEPH detector. The sense wires were made of gold plated tungsten and were grouped in eight concentric layers, all of them parallel to the beam direction. The total acceptance of particles passing through the eight sets of wires was between 14^o to 165^o.

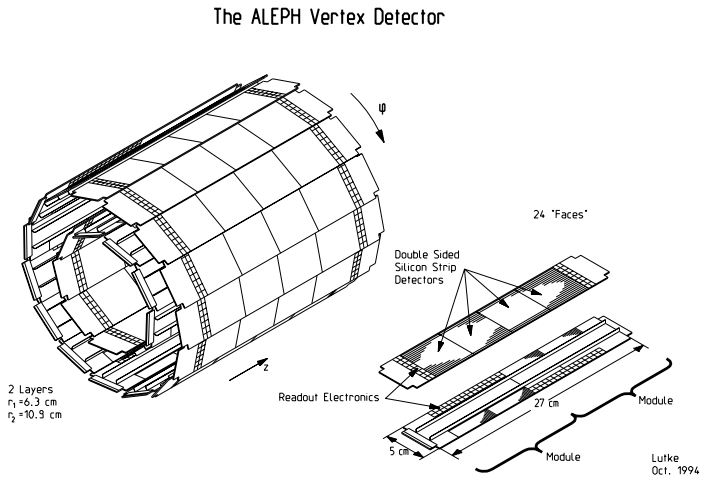

Figure 3.4: The original (1991) VDET configuration.

It had two main purposes in ALEPH. One was giving tracking information in the level 1 trigger (about 2-3 μs after the collision time). A second purpose was reconstructing the direction of charged tracks as part of the total tracking system, providing up to 8 points. The z information from the ITC was not used, but for $r\phi$ the precision of each point was about 150 μm.

The ITC has also been used for the $\tau^+\tau^-$ event selection in rejecting the cosmic background [34]. Most of the cosmic events have less than 6 ITC points due to the uncorrelation in time with the beam–crossing.

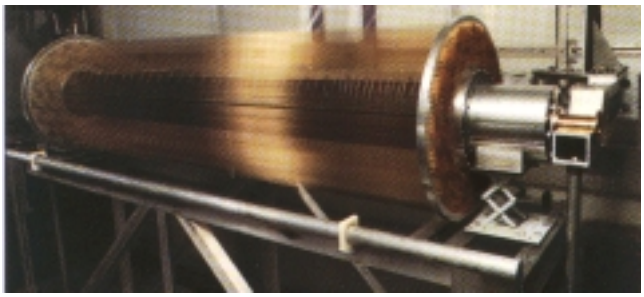

Figure 3.5: An overall view of the ITC.

3.2.3 TPC

The TPC was the main ALEPH tracking device. It was an imaging drift chamber, 4.7 m long, with an inner radius of 35 cm and with an outer radius of 180 cm. An overall view of this device can be seen in fig. 3.6. It was filled with a non–flammable mixture of $Ar(91\%)$ and $CH_4(9\%)$ at atmospheric pressure.

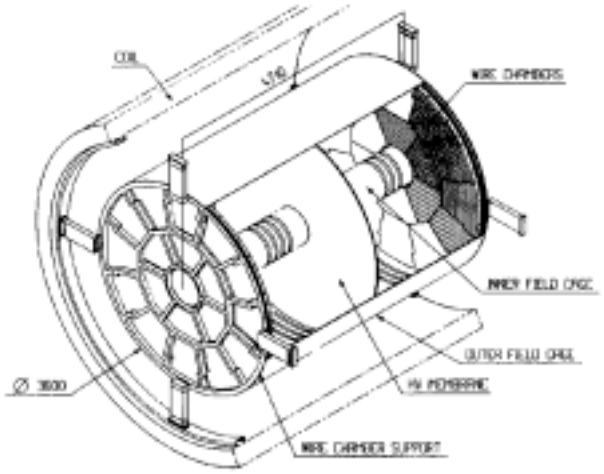

Figure 3.6: Overall view of the TPC.

An electric field of 110 V/cm parallel to the beam direction was pointing from each end–plate towards the central membrane, dividing the chamber into two halves. The end–plates were divided into sectors: 6 inner sectors, called K–sectors, and 12 outer sectors, with M and W alternating sectors (see fig. 3.7). In these sectors, every wire chamber provided the readout of the energy depositions.

A charged particle traversing the chamber ionises the medium, and the ionisation electrons drift parallel to the electric field direction towards the end–plates. The ionisation electrons described a spiral trajectory in their movement towards the end–plates, due to the presence of the 1.5 T magnetic field generated by the Superconducting Coil. This spiral trajectory had the advantage of reducing the diffusion in the drift towards the end–plates.

A charged track could give a maximum of 27 hits with three–dimensional information (8 from the inner sectors and 19 from the outer sectors). The $r\phi$ coordinates